Inorganic Chemistry

Article

pubs.acs.org/IC

Distinct Photophysics of the Isomers of $B_{18}H_{22}$ Explained

Michael G. S. Londesborough,*[,†] Drahomír Hnyk,*[,†] Jonathan Bould,[†] Luis Serrano-Andrés,[‡] Vicenta Sauri,[‡] Josep M. Oliva,*[,§] Pavel Kubát,[∥] Tomáš Polívka,[⊥] and Kamil Lang*[,†]

[†]Institute of Inorganic Chemistry of the AS CR, v.v.i., 250 68 Husinec-Řež, Czech Republic

[‡]Instituto de Ciencia Molecular, Universitat de València, Valencia, Spain

[§]Instituto de Química Física "Rocasolano", CSIC, Madrid, Spain

[∥]J. Heyrovský Institute of Physical Chemistry of the AS CR, v.v.i., Dolejškova 3, 182 23 Praha 8, Czech Republic

[⊥]Institute of Physical Biology, University of South Bohemia, Zámek 136, 373 33 Nové Hrady, Czech Republic

Supporting Information

ABSTRACT: The photophysics of the two isomers of octadecaborane(22), *anti*- and *syn*-$B_{18}H_{22}$, have been studied by UV−vis spectroscopic techniques and theoretical computational methods. In air-saturated hexane, *anti*-$B_{18}H_{22}$ shows fluorescence with a high quantum yield, $\Phi_F = 0.97$, and singlet oxygen $O_2(^1\Delta_g)$ production ($\Phi_\Delta \sim 0.008$). Conversely, isomer *syn*-$B_{18}H_{22}$ shows no measurable fluorescence, instead displaying much faster, picosecond nonradiative decay of excited singlet states. Computed potential energy hypersurfaces (PEHs) for both isomers rationalize these data, pointing to a deep S_1 minimum for *anti*-$B_{18}H_{22}$ and a conical intersection (CI) between its S_0 and S_1 states that lies 0.51 eV higher in energy. Such an energy barrier to nonradiative relaxation is not present in the PEH of *syn*-$B_{18}H_{22}$, and the system therefore has sufficient initial energy on excitation to reach the (S_0/S_1) CI and to then decay to the ground state without fluorescence. The computational analysis of the geometries at stationary points along the PEH of both isomers shows that the determining factor for the dissimilar photophysics of *anti*- and *syn*-$B_{18}H_{22}$ may be due to the significant differences in the geometrical rearrangements at their respective conical intersections. Thus, the *syn* isomer shows one very large, B−B elongation of 1.2 Å from 1.8 Å in the ground state to 3.0 Å at the CI, whereas the *anti* isomer shows smaller elongations (below 1 Å) in several B−B connectivities at its $(S_0/S_1)_{CI}$. The absorbed energy in S_1 for the *anti*-$B_{18}H_{22}$ is therefore redistributed vibrationally into several regions of the molecule rather than almost completely into a single vibrational mode as in the case for the *syn* isomer. The consequent prolonged S_1 lifetime for the *anti* isomer allows for relaxation via fluorescence.

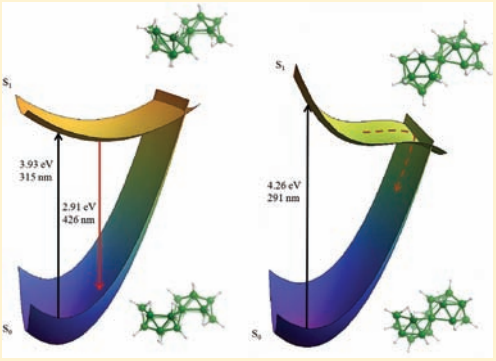

INTRODUCTION

The *anti*- and *syn*-isomers of octadecaborane(22), prized for their high molecular boron content, ready synthesis, and stability in air, are two of the more important binary boron hydrides available for practical applications. In recent years they have received particular attention from the semiconductor industry as new-generation dopant materials used in the fabrication of *p*-type silicon. As a dopant, octadecaborane(22) makes shallow boron implants into silicon wafers at high throughputs and low energies, which are significant industrial advantages.[1] Running parallel to the development of this technology is the requirement to better understand the chemistry and physics of octadecaborane(22) at fundamental levels.

In this context we have become interested in the physicochemical differences between the two isomers of $B_{18}H_{22}$, and we have, for example, recently published a conversion route from *syn*- to *anti*-$B_{18}H_{22}$ via their common $[B_{19}H_{22}]^-$ anion.[2] Both the *syn*- and *anti*-$B_{18}H_{22}$ isomers are structurally related to commercially available decaborane(14). The structure of *syn*-$B_{18}H_{22}$ can be formally derived from the fusion of two $\{B_{10}\}$ units which share a common B−B edge so that the molecule has a 2-fold axis of symmetry (Figure 1A). In the case of the *anti*-$B_{18}H_{22}$ isomer, the two halves of the molecule are related by a center of symmetry (Figure 1B).

Hawthorne, to whom much of the early work on the chemistries of octadecaborane(22) can be credited, noted the absorption spectra of *syn*- and *anti*-$B_{18}H_{22}$ in the UV−vis region.[3] However, besides the simple documentation of the absorption bands, useful for compound identification, and the note that "solutions of the hydride in hydrocarbon solvents exhibit a purple fluorescence" (no emission spectra were reported), there has been no further consideration of this interesting property. This is somewhat surprising as visible fluorescence is, as far as we are aware, a unique property in the neutral binary boron hydrides although some pyridine derivatives of other cluster boranes and carboranes have been

Received: August 8, 2011
Published: January 6, 2012

   dx.doi.org/10.1021/ic201726k | *Inorg. Chem.* 2012, 51, 1471−1479

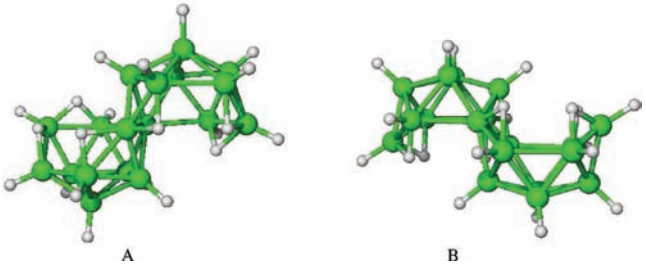

Figure 1. Molecular structures of *syn*-$B_{18}H_{22}$ (A) and *anti*-$B_{18}H_{22}$ (B) isomers. For numbering see Figure 7.

reported to be luminescent under UV irradiation.[4] Furthermore, the fluorescence is observed only in *anti*-$B_{18}H_{22}$ and is absent in similar solutions of *syn*-$B_{18}H_{22}$. This interesting difference between the two isomers is deserving of closer investigation, especially due to our interest in the physicochemical differences between the two isomers of $B_{18}H_{22}$. Thus, in order to gain a deeper insight into the electronic structure of the two isomers and to find an explanation for the distinctive fluorescence behavior of the isomers, we embarked on a UV−vis spectroscopic study of both species using contemporary time-resolved techniques, which are verified and supplemented by the employment of sophisticated computational methods.

EXPERIMENTAL SECTION

The two isomers of $B_{18}H_{22}$ were synthesized from the hydrolysis of the hydronium ion salt of $[B_{20}H_{18}]^{2-}$ according to the method described in the literature.[3] Pure samples of each isomer were obtained by repeated crystallizations from hot saturated *n*-hexane solutions and had ^{1}H and ^{11}B NMR and mass spectroscopic characteristics in agreement with the published data.[3,5]

Hexane (Spectranal, Riedel-de Haën) and chloroform (HPLC grade, Aldrich) were used for the preparation of all solutions used for UV−vis spectroscopic measurements, which were carried out with a PerkinElmer Lambda 35 spectrometer. Luminescence properties were monitored on a Fluorolog 3 spectrometer (Horiba Jobin Yvon). Emitted light was detected either using a cooled TBX-05-C photon detection module (fluorescence) or was filtered by a Shott RG 830 glass filter and detected using a Hamamatsu H10330-45 photomultiplier (phosphorescence of $O_2(^1\Delta_g)$). Time-correlated single photon counting measurements were performed using an excitation wavelength of 370 nm (laser diode IBH NanoLED, repetition rate 1 MHz, peak wavelength 370 nm, pulse width 0.1 ns) at room temperature. Emission from the sample was recorded at 420 nm using a cooled TBX-05-C photon detection module. Additionally, a 590 nm cut-on filter was used to eliminate scattered light and the data were collected until the peak value reached 10 000 counts. The decay curves were fitted to exponential functions using an iterative reconvolution procedure of the DAS6 software (v. 6.4, Horiba Jobin Yvon, 2009). In the case of time-resolved $O_2(^1\Delta_g)$ measurements the sample was excited by a 355 nm laser (Crylas, FTSS 355−50) and emission was detected at 1275 nm using a Hamamatsu H10330−45 photomultiplier.

The fluorescence quantum yield of *anti*-$B_{18}H_{22}$, Φ_F, in hexane was measured by the comparative method with quinine sulfate as a reference (0.1 M H_2SO_4, oxygen-free, λ_{exc} = 350 nm, Φ_F^R = 0.58).[6] The absorptions were kept below 0.05 in 10 mm × 10 mm quartz cells. The quantum yield was calculated using

$$\Phi_F = \Phi_F^R \left(\frac{F}{F^R}\right)\left(\frac{A^R}{A}\right)\left(\frac{n}{n^R}\right)^2 \quad (1)$$

where F is the integrated area under the emission spectrum, A is absorbance at the excitation wavelength, and n is the respective refractive index of the solvent. Superscript R corresponds to the reference.

Femtosecond transient absorption data were obtained with a 1 kHz femtosecond laser system (Integra-I, Quantronix) providing ∼130 fs pulses with an average energy of ∼2 mJ/pulse, and a central wavelength of 790 nm. The pulses were divided into two paths serving as excitation and probe pulses. The major part for generation of excitation pulses was directed to the optical parametric amplifier TOPAS, in which 330 nm excitation pulses were produced by fourth harmonic generation of TOPAS signal. A white-light continuum, obtained by focusing a fraction of the 790-nm pulses into a 0.2 cm sapphire plate, was used for probing. For signal detection, the probe beam and an identical reference beam were focused onto the entrance slit of a spectrograph, which then dispersed both beams onto a dual photodiode array detection system (ExciPro, CDP Systems). A 1-mm path length rotating quartz cell spinning at a rate ensuring that each excitation pulse hits a fresh sample was used for measurements. The mutual orientation of the excitation and probe beams was set to the magic angle (54.7°). The lifetime of the *syn*-$B_{18}H_{22}$ excited states was obtained from global fitting of the whole spectro-temporal data set.

Time-resolved near-infrared phosphorescence of $O_2(^1\Delta_g)$ at 1270 nm was monitored with a germanium diode Judson J16-8SP-R05M-HS, in conjunction with a 1270 nm band-pass filter (Laser Components, Olching, Germany). The sample was excited by a Lambda Physik COMPEX 102 excimer laser (308 nm, 28 ns, ∼1−5 mJ/pulse). All traces were accumulated 50−100 times to improve the signal-to-noise statistics. The experiments were performed in argon-, air-, or oxygen-saturated solutions. The phosphorescence signal of $O_2(^1\Delta_g)$ contained a short-lived signal caused by scattering of the excitation laser pulse. This signal was eliminated by exciting the sample in the absence of O_2 (argon-saturated solution) and by subtracting the obtained signal from the signal recorded in an oxygen-containing solution. The averaged kinetic traces were fitted by the following fitting function with τ_T (triplet states lifetime), τ_Δ (lifetime of $O_2(^1\Delta_g)$), and A (amplitude) as free parameters:

$$S(t) = A\frac{\tau_\Delta}{\tau_T - \tau_\Delta}(\exp(-t/\tau_T) - \exp(-t/\tau_\Delta)) \quad (2)$$

The quantum yield of singlet oxygen formation, Φ_Δ, in hexane was estimated by the comparative method using 5,10,15,20-tetraphenylporphyrin (TPP, Φ_Δ = 0.6 in benzene)[7] as a standard. The absorbances of air-saturated solutions of sample and reference were A_{308} = 0.322 ± 0.002. At each energy density, sufficiently low to keep the plot amplitude versus energy density linear, the recorded phosphorescence trace was obtained by the signal averaging of 500 single shots. The ratio of the zero-time extrapolated amplitude of the $O_2(^1\Delta_g)$ single-exponential decay for sample and reference affords the ratio of quantum yields. Saturating the solutions with O_2 did not change the results.

Attempts to record time-resolved absorption changes on a microsecond time scale were performed using a LKS 20 (Applied Photophysics, U.K.) laser kinetic spectrometer equipped with a 250 W Xe lamp, a pulse unit, and an R928 photomultiplier (Hamamatsu) within a 300−850 nm range. A Lambda Physik COMPEX 102 laser was used as the excitation source (308 nm, 28 ns fwhm, 2−50 mJ/pulse).

THEORETICAL METHODOLOGY

In the theoretical calculations, both density functional theory (DFT) and *ab initio* multiconfigurational methods were used. The complete active space self-consistent field (CASSCF) approach followed by multireference second-order perturbation theory (CASPT2) was used to compute potential energy hypersurfaces (PEH) minima and crossings, together with state and transition properties for the lowest-lying singlet and triplet states of both $B_{18}H_{22}$ isomers. The ground (S_0) and low-lying triplet (T_1) state minima were optimized and characterized at the DFT/B3LYP/6-31+G(d) level of theory. All other calculations, including determinations of PEH minima and crossings, were performed with the CASSCF method supplemented, at

dx.doi.org/10.1021/ic201726k | Inorg. Chem. 2012, 51, 1471−1479

Table 1. Photophysical Properties of *syn*-$B_{18}H_{22}$ and *anti*-$B_{18}H_{22}$ in Air-Saturated Hexane: Absorption Spectra (Molar Absorption Coefficients ε at Band Maxima λ_{max}), Fluorescence Band Maximum λ_F, Quantum Yield of Fluorescence Φ_F, Lifetime of the Excited Singlet States τ_F, Quantum Yield of the Triplet States Φ_T, Lifetime of the Triplet States τ_T, Quantum Yield of Singlet Oxygen Formation Φ_Δ

		excited singlet states			triplet states		
$B_{18}H_{22}$ isomer	absorption spectra λ_{max}/nm (ε/mM^{-1}cm^{-1})	λ_F/nm	Φ_F	τ_F/ns	Φ_T	τ_T/μs	$O_2(^1\Delta_g)$ Φ_Δ
syn	229 (7.32), 308 (8.66)		~0[a]	0.075[b]		<2[c]	~0.008[c]
anti	215 (15.2), 272 (3.36), 329 (6.29)	407[a]	0.97 ± 0.02[a]	11.2 ± 0.1[a]	<0.03[a]	6 ± 2[c]	~0.008[c]

[a]Data from fluorescence emission spectroscopy. [b]Data from femtosecond transient absorption spectroscopy. [c]Data from time-resolved near-infrared phosphorescence of $O_2(^1\Delta_g)$.

the obtained points, with CASPT2 calculations in order to include the necessary dynamical correlation effects. The protocol is usually named CASPT2//CASSCF,[8] and has proven its accuracy repeatedly.[9] The conical intersection structures were determined as minimum energy crossing points (MECP) between the two states involved. The one-electron atomic basis set 6-31+G(d) was used throughout. Unless otherwise specified the final results use an active space of 12 molecular orbitals and 12 electrons. No symmetry restrictions were imposed during the calculations. At the ground state, the *anti*-$B_{18}H_{22}$ and *syn*-$B_{18}H_{22}$ isomers were determined to have C_i and C_2 geometries, respectively, and therefore, the corresponding state labeling is used when required. From the calculated CASSCF transition dipole moments (TDM) and the CASPT2 excitation energies, oscillator strengths and radiative lifetimes have been obtained, the latter using the Strickler–Berg relationship,[10] which is valid under the hypothesis that excited state nonradiative deactivation is of minor importance. Spin–orbit coupling (SOC) terms between singlet and triplet states were computed within the AMFI and CASSI frameworks,[11] as described in the Supporting Information. Test calculations made to check the reliability of the results employing larger active spaces and basis sets, or substituting S_0 and T_1 optimized geometries by CASSCF structures, were performed, as described in the different sections and the Supporting Information. In all cases the results in excitation energies were shown to fall within the expected 0.1–0.2 eV accuracy. Calculations employed the Gaussian03[12] (DFT) and the MOLCAS-7[13] (CASSCF/CASPT2) sets of programs. Additional technical details can be found in the Supporting Information, together with the selected geometries computed for the different systems.

RESULTS AND DISCUSSION

Experimental Results. The absorption spectrum of *anti*-$B_{18}H_{22}$ in hexane is characterized by broad bands at 272 and 329 nm that are bathochromically shifted to 229 and 308 nm for the *syn*-$B_{18}H_{22}$ isomer (Table 1, Figure S1 in the Supporting Information). Both isomers differ considerably in their fluorescence properties (Table 1). *anti*-$B_{18}H_{22}$ shows very strong fluorescence peaking at 407 nm in hexane (Figure S1 in the Supporting Information) with a fluorescence quantum yield, Φ_F, of 0.97 ± 0.02 and a relatively long fluorescence lifetime of 11.2 ± 0.1 ns. The superimposition of the excitation spectra and the absorption spectra serves as an experimental confirmation of the identity of the fluorescence. The energy level of the lowest singlet excited state was estimated from the intersection of the normalized absorption and emission bands, giving a value of 3.41 eV. In contrast, *syn*-$B_{18}H_{22}$ has no detectable fluorescence emission.

Femtosecond transient absorption spectroscopy was used to detect nonemitting transients produced upon excitation of *syn*-$B_{18}H_{22}$. Femtosecond flash excitation at 330 nm of *syn*-$B_{18}H_{22}$ in hexane affords the absorption profile of the excited singlet state with a maximum at 475 nm (Figure 2b). Fast relaxation to the ground state with a time constant of about 75 ps (Figure S2 in the Supporting Information) is in accordance with the

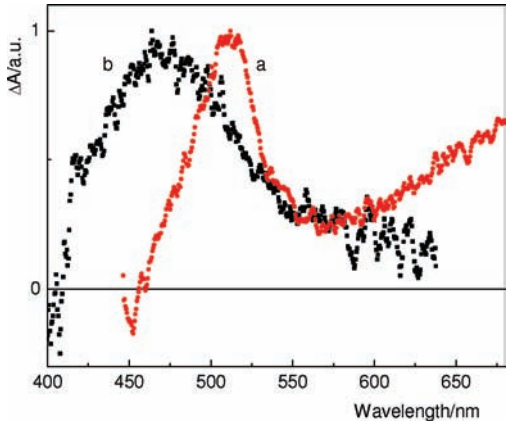

Figure 2. Transient absorption spectra of *anti*-$B_{18}H_{22}$ (a) and *syn*-$B_{18}H_{22}$ (b) excited at 330 nm and recorded at 100 and 12 ps, respectively.

nonfluorescent character of *syn*-$B_{18}H_{22}$. For comparison, the excited singlet states of *anti*-$B_{18}H_{22}$ are characterized by a narrow band at 512 nm and broad absorption above 600 nm (Figure 2a). The kinetics recorded at 512 nm does not decay within the time window of the femtosecond experiment (Figure S2 in the Supporting Information), in agreement with the 11.2 ns lifetime obtained by the fluorescence decay analysis (Table 1).

The observed phosphorescence at 1270 nm, which may be attributed to $O_2(^1\Delta_g)$ (Figure 3, inset), appears after excitation

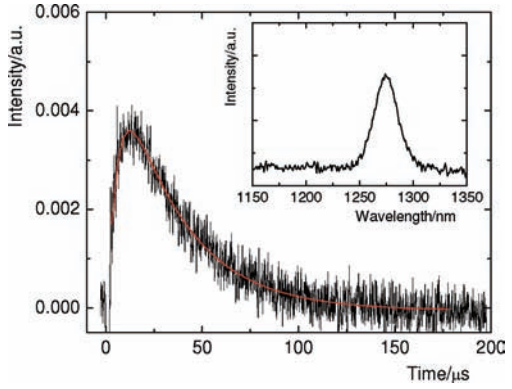

Figure 3. Time dependence of the $O_2(^1\Delta_g)$ phosphorescence at 1270 nm produced by *anti*-$B_{18}H_{22}$ (λ_{exc} = 308 nm) calculated as the difference of the signal in air- and argon-saturated hexane. The smoothed red line is a least-squares fit to the pure luminescence signal (eq 2). Inset shows phosphorescence spectrum of $O_2(^1\Delta_g)$ in an oxygen-saturated chloroform solution of *anti*-$B_{18}H_{22}$ (λ_{exc} = 350 nm).

dx.doi.org/10.1021/ic201726k | Inorg. Chem. 2012, 51, 1471–1479

Table 2. Theoretical (CASPT2) Absorption and Emission Spectra of *anti*-$B_{18}H_{22}$

	CASPT2							
state	E_{VA}[a] /eV	λ_{VA}[a] /nm	f[a]	T_e[a] /eV	λ_e[a] /nm	E_{VE}[a] /eV	λ_{VE}[a] /nm	τ^o/s
1^1A_u	3.93	315	0.265	3.63[c]	341[c]	2.91[c]	426[c]	5.6×10^{-9}
2^1A_u	4.99	248	0.051					
4^1A_u	5.85	212	0.884					
1^3A_u	3.48	356		3.04	408	2.49	498	0.51
2^3A_u	4.63	268						
	experimental							
	A_{max}[b] /eV	λ_{amax}[b] /nm	f[d]	T_0[b] /eV	λ_0[b] /nm	E_{max}[b] /eV	λ_{emax}[b] /eV	τ^o/s
1^1A_u	3.77	329	~0.4	3.41	364	3.05	407	1.2×10^{-8}
2^1A_u	4.56	272	~0.2					
4^1A_u	5.76	215	~1.0					

[a]Computed vertical absorption energy (E_{VA}) and wavelength (λ_{VA}), electronic band origin energy (T_e) and wavelength (λ_e), vertical emission energy (E_{VE}) and wavelength (λ_{VE}), oscillator strength (f), natural radiative lifetime (τ^o). [b]Experimental absorption band maxima energy (A_{max}) and wavelength (λ_{amax}), band origin energy (T_0) and wavelength (λ_0), emission band maxima energy (E_{max}) and wavelength (λ_{emax}) in hexane. [c]Maximum of the transient absorption experiments: 2.42 eV (512 nm). At the 1^1A_u optimized geometry the most intense transition from 1^1A_u is computed to the 7^1A_g state at 2.69 eV with oscillator strength 0.352. [d]Normalized using molar absorption coefficients.

of both isomers, disappears after purging the sample with argon, and reappears after the addition of air or oxygen (Figures S3 and S4 in the Supporting Information). The steep increase in the $O_2(^1\Delta_g)$ concentration during the first 10 μs after excitation of *anti*-$B_{18}H_{22}$ hexane solutions (Figure 3) suggests that $O_2(^1\Delta_g)$ is formed by the diffusion-controlled quenching of the excited states by oxygen, although a contribution from $O_2(^1\Delta_g)$ produced by photodecomposition of a boron cluster-O_2 adduct[14] cannot be excluded. The formation of $O_2(^1\Delta_g)$ from excited singlet states is not expected as fluorescence of *anti*-$B_{18}H_{22}$ is not quenched by oxygen within experimental error, and *syn*-$B_{18}H_{22}$ has a very short lifetime in its singlet excited states (τ_F = 75 ps). We therefore suggest that the triplet states are involved in the formation of $O_2(^1\Delta_g)$.

The lifetime of the *anti*-$B_{18}H_{22}$ $O_2(^1\Delta_g)$-producing states calculated from phosphorescence decay at 1270 nm (eq 2) is τ_T = 6 ± 2 μs in air-saturated hexane (Figure 3). The obtained value of τ_Δ = 32 ± 4 μs is in good agreement with the lifetime of $O_2(^1\Delta_g)$ in pure hexane (~30 μs).[15] For comparison, the lifetime of these states is longer in chloroform (τ_T = 13 μs), concomitant with the longer lifetime of $O_2(^1\Delta_g)$ (τ_Δ = 170 μs) in chloroform. In the case of *syn*-$B_{18}H_{22}$ the lifetime of the triplet states is shorter than 2 μs and cannot be directly measured as the rise of the signal overlaps with an initial light scattering peak (Figure S3 in the Supporting Information). We estimate the quantum yield of $O_2(^1\Delta_g)$ formation to be Φ_Δ ~ 0.008 for both the *anti*-$B_{18}H_{22}$ and *syn*-$B_{18}H_{22}$ isomers.

Despite several attempts, no transient absorptions were observed on a microsecond time scale. The fact that the absorption of the $O_2(^1\Delta_g)$-producing states and their quenching by molecular oxygen was not observed can be explained by the very low quantum yield of the triplet state formation (<0.03) and low triplet(1^3A_u)−triplet oscillator strengths (Table S1 in the Supporting Information) in the case of *anti*-$B_{18}H_{22}$ and the fast relaxation of the excited states and very low triplet(1^3B)−triplet oscillator strengths (Table S2 in the Supporting Information) in the case of *syn*-$B_{18}H_{22}$.

Calculations and Comparison with Experimental Data. *Absorption Spectra.* Selected CASSCF/CASPT2 calculated and the measured experimental data for the absorption spectrum of *anti*-$B_{18}H_{22}$ are compiled in Table 2 (full list of data in Table S1, Supporting Information). The ground state (S_0) minimum geometry, determined to belong to the C_i point group symmetry at the B3LYP level and therefore labeled 1^1A_g, has been employed. Several intense transitions have been computed from the ground state 1^1A_g up to 183 nm (6.76 eV) toward one-photon allowed ^1A_u states, two of which fall within the boundaries of the recorded experimental data in hexane, up to 200 nm (6.20 eV). As is typical in many organic systems, the low-lying spectra of the molecule, especially its most intense bands, can be mainly described by the four Platt-type states[16] relating the four highest occupied and lowest unoccupied molecular orbitals: the ^1L_a state, basically described as the HOMO (H) → LUMO (L) one-electron promotion; the ^1L_b and ^1B_b states, the respective antisymmetric (low intensity) and symmetric (high intensity) combination of the H − 1 → L and H → L+1 configurations; and the ^1B_a state, described by the H − 1 → L + 1 one-electron promotion (Figure 4). The

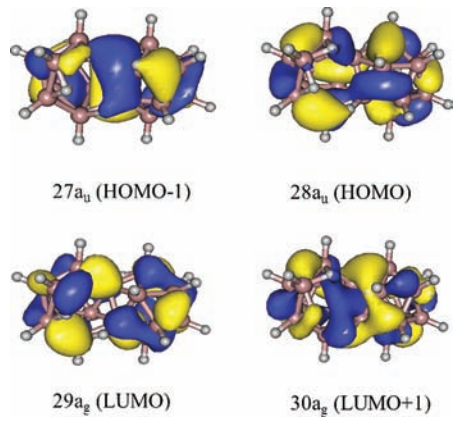

Figure 4. Most relevant CASSCF molecular orbitals for the *anti*-$B_{18}H_{22}$ isomer.

lowest-energy singlet−singlet transition, $1^1A_g \rightarrow 1^1A_u$, described as the H → L one-electron promotion (90%) at the CASSCF level, is computed vertically at 315 nm (3.93 eV) with an oscillator strength of 0.265, and it can be clearly assigned to the band maximum observed for the *anti* isomer at 329 nm (3.77 eV) with an intermediate intensity. Figure 4 displays the most relevant CASSCF molecular orbitals for the *anti*-$B_{18}H_{22}$ isomer,

dx.doi.org/10.1021/ic201726k | Inorg. Chem. 2012, 51, 1471−1479

Table 3. Theoretical (CASPT2) Absorption and Emission Spectra of *syn*-$B_{18}H_{22}$

	CASPT2							
state	E_{VA}[a] /eV	λ_{VA}[a] /nm	f[a]	T_e[a] /eV	λ_e[a] /nm	E_{VE}[a] /eV	λ_{VE}[a] /nm	τ_{rad}/s
1^1B	4.26	291	0.338	4.03[c]	308[c]	3.36[c]	369[c]	
4^1A	5.56	223	0.158					
3^1B	5.76	215	0.251					
1^3B	3.76	329		3.31	375	2.67	464	0.96
1^3A	4.13	300						
	experimental							
	A_{max}[b] /eV	λ_{amax}[b] /nm	f[d]					
1^1B	4.03	308	~0.6					
4^1A, 3^1B	5.41	229	~0.5					

[a]Computed vertical absorption energy (E_{VA}) and wavelength (λ_{VA}), electronic band origin energy (T_e) and wavelength (λ_e), vertical emission energy (E_{VE}) and wavelength (λ_{VE}), oscillator strength (f), radiative lifetime (τ_{rad}). [b]Experimental absorption band maxima energy (A_{max}) and wavelength (λ_{amax}) in hexane. [c]The minimum was found along the relaxation path of the 1^1B state only by restricting the symmetry to C_2. Otherwise, the optimization leads directly to the crossing with the ground state $(S_0/S_1)_{CI}$. No fluorescence emission is therefore expected. [d]Normalized using molar absorption coefficients.

which are shown to be distributed along the structure of the borane cage. Next, a transition to the 2^1A_u state is computed at 248 nm (4.99 eV), described essentially as a combination of two configurations, H − 1 → L (74%) and H → L + 1 (16%), and with a related oscillator strength of 0.051. As no other intense transition has been computed in the 310−225 nm (4.0−5.5 eV) energy interval, this can be unambiguously assigned to the weak and broad band peaking at 272 nm (4.56 eV). It is not surprising that the theoretically computed excitation energies ("vertical" absorption energies), which are derived from using the ground state optimized geometry, lie higher in energy than the measured band maxima. This is because the equilibrium geometries of the excited states are different from that of the ground state, and, with regard to the Franck−Condon principle, the verticality of the transitions is only partially fulfilled.

Apart from the computed weak transition for the 3^1A_u state at 223 nm (5.55 eV), which lies beneath the most intense measured band at 215 nm (5.76 eV), only one other allowed transition has been computed within the range of the experimental spectrum. This is the 4^1A_u state at 212 nm (5.85 eV), which has a large oscillator strength (0.884) and may be assigned to the measured feature at 215 nm (5.76 eV). In turn, this feature can be described as ^1B_b; i.e., the counterpart of the 2^1A_u (^1L_b) transition according to its CASSCF wave function: H − 1 → L (15%) and H → L + 1 (70%). A further two allowed transitions have been obtained at 186 nm (6.65 eV) and 183 nm (6.76 eV), the highest with a large oscillator strength of 0.746 and described by the H → L + 1 (48%) configuration. Additionally, nine states of both ^3A_g and ^3A_u symmetry have been computed in the energy range 356−215 nm (3.48−5.76 eV). The two lowest singlet−triplet transitions have been obtained toward the 1^3A_u and 2^3A_u states at 356 nm (3.48 eV) and 268 nm (4.63 eV), described by the H → L and H → L + 1 configurations, respectively. Only one triplet state therefore lies below the lowest singlet−singlet transition. The spin−orbit coupling (SOC) terms obtained between singlet and triplet states were, in general, large (from 3 to 5 cm^{-1}) for states of the same spatial symmetry. If we focus, however, on the low-energy region of the spectrum where only the 1^1A_u state becomes largely populated, the closest-lying triplet states lie more than 0.5−0.7 eV away in energy, making the energy gap too large to expect an efficient intersystem crossing process at the ground-state Franck−Condon (FC) region. This process can be, however, enhanced in other areas of the PEH.

Tables 3 and S2 (Supporting Information) compile the CASSCF/CASPT2 results and experimental data related to the absorption spectrum of the *syn*-$B_{18}H_{22}$ system, which displays a C_2 point group symmetry for its ground (S_0) state (1^1A) minimum at the B3LYP level of calculation. The *syn* isomer was found to be 0.42 eV (9.7 kcal mol^{-1}) less stable than the *anti* counterpart at the CASPT2 level of calculation. The two medium-intensity bands observed in the UV absorption spectrum in hexane at 308 nm (4.03 eV) and 229 nm (5.41 eV) can be assigned to the lowest-lying transition to the 1^1B and 3^1B states computed at 291 nm (4.26 eV) and 215 nm (5.76 eV) with oscillator strengths 0.338 and 0.251, respectively. According to their CASSCF wave function, these two states can be made to correspond to Platt's ^1L_a (H → L 85%) and ^1B_a (H − 1 → L + 1 74%) states. With regard to Platt's *b*-type states, in this system the mixture takes place for the 3^1A and 4^1A states between the H → L + 2 and H − 2 → L configurations. Figure 5 displays the corresponding CASSCF molecular orbitals. Other transitions will contribute to a lesser extent to the band's intensity, such as the excitation to the 4^1A state at 223 nm (5.56 eV), which also displays a large oscillator strength and presumably participates in the 229 nm band. In the experimental spectrum (Figure S1 in the Supporting Information) there is an intense band peaking at energies

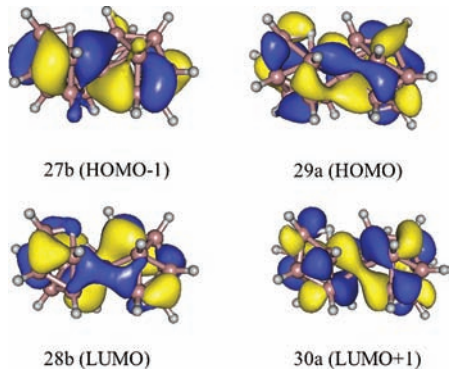

Figure 5. Most relevant CASSCF molecular orbitals for the *syn*-$B_{18}H_{22}$ isomer.

dx.doi.org/10.1021/ic201726k | *Inorg. Chem.* 2012, 51, 1471−1479

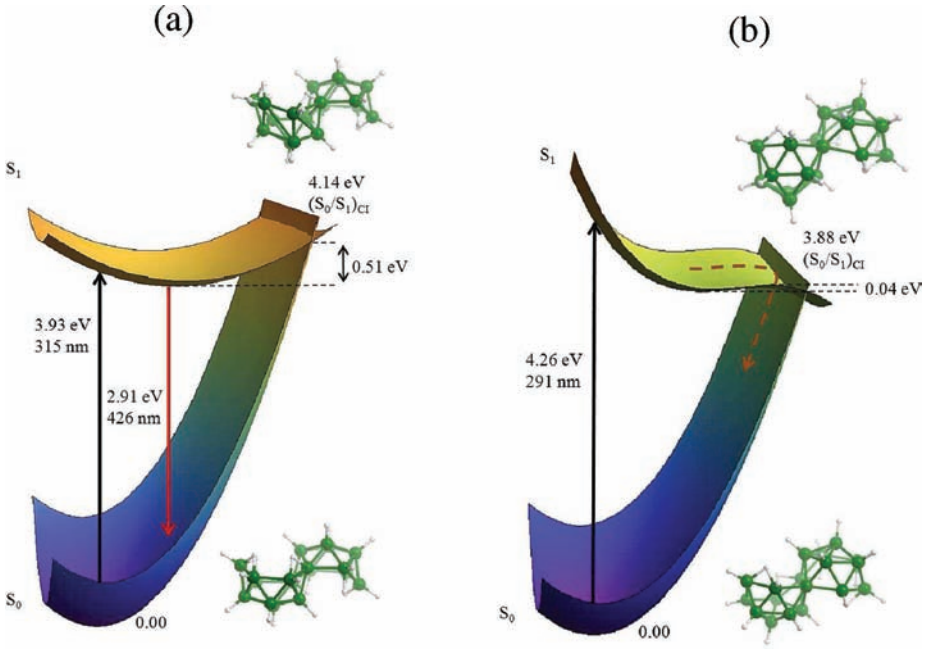

Figure 6. Photophysics, potential energy hypersurfaces, and structures of the ground state (S_0) and first excited singlet state (S_1) for (a) *anti*-$B_{18}H_{22}$ and (b) *syn*-$B_{18}H_{22}$ based on experimental and CASPT2 results.

higher than 200 nm (6.2 eV), which corresponds to the series of intense transitions computed in the 190 nm (6.5 eV) region (Table S2 in the Supporting Information). In contrast to the apolar *anti*-$B_{18}H_{22}$ isomer, the C_2 symmetry *syn*-$B_{18}H_{22}$ species has a polar character. The dipole moment of the ground state is computed to be 2.45 D, higher than for any of the singlet states computed below 6 eV. Corresponding blue-shifts can be therefore expected for the observed absorption bands, although the lowest-lying feature to the 1^1B state (having a dipole moment of 2.12 D) will not be strongly affected. A number of triplet excited states have also been computed for *syn*-$B_{18}H_{22}$. In this case, two triplet-transitions lie below the lowest-lying singlet state at 291 nm (4.26 eV): the $1^1A \rightarrow 1^3B$ transition at 329 nm (3.76 eV) and the $1^1A \rightarrow 1^3A$ at 300 nm (4.13 eV). In general, and except for the interaction between the ground singlet and the triplet states, the singlet−triplet SOC elements are smaller for the *syn*-$B_{18}H_{22}$ than for the *anti*-$B_{18}H_{22}$ isomer. In the FC region, however, there is a small gap between the most populated state of the low-energy tail of the spectrum, 1^1B, and the 1^3A state (0.13 eV). These states display a SOC term of 1.2 cm^{-1}, which, combined with the small energy gap, indicates a potential channel for ISC transfer toward the triplet manifold in this area of the PEH.

Fluorescence. Tables 2 and 3 compile the most important computed (CASPT2) and experimental data describing the photophysics of the two *anti* and *syn* isomers of $B_{18}H_{22}$, including absorption, emission, and decay properties. Figure 6 summarizes the proposed photophysics based on our experimental and computed results. Regarding the *anti*-$B_{18}H_{22}$ isomer, one excited state of singlet nature and another of triplet character seem to be the main protagonists of its photophysics in the low-energy region of the spectrum. After being populated, the system in the 1^1A_u (S_1) state is expected to evolve toward the state minimum, computed adiabatically (T_e, electronic minimum of S_0 to electronic minimum of S_1) at 341 nm (3.63 eV). This energy corresponds to the band origin, both for the absorption and emission band (except for the solvent effects) measured around 364 nm (3.41 eV) in hexane (Figure S1 in the Supporting Information, Table 2). The emission energy computed from the S_1 state minimum vertically to the S_0 state at 426 nm (2.91 eV) nicely agrees with the fluorescence emission maximum observed at 407 nm (3.05 eV). As *anti*-$B_{18}H_{22}$ yields an intense emission, the Strickler−Berg approximation[10] can be safely applied to compute the natural radiative lifetime of $\tau^o = 5.6 \times 10^{-9}$ s, a time short enough to correspond to an intensely absorbing state such as 1^1A_u. The experimental τ^o can be calculated using the equation τ_F/Φ_F, to give 1.2×10^{-8} s, a value that is not very far from the calculated natural lifetime.

The presence of a minimum along the main decay pathway of the S_1 state is an initial indication of the intrinsic emissive character of *anti*-$B_{18}H_{22}$ and the relatively long lifetime of the state. Indeed, time-resolved fluorescence and femtosecond transient absorption experiments recorded in hexane at 512 nm (2.42 eV) demonstrate a slow 11.2 ns decay for *anti*-$B_{18}H_{22}$, whereas the *syn* species has a corresponding absorption at 475 nm (2.61 eV), and a comparatively much faster S_1 decay of 75 ps (Figures 2 and S2 in the Supporting Information). The short lifetime in the latter case is in agreement with the lack of fluorescence emission, pointing to fast internal conversion toward the ground state within *syn*-$B_{18}H_{22}$. The differing photophysics of the two isomers can be directly rationalized through the PEH decay profiles along the spectroscopic S_1 state (Figure 6). Modern photochemistry relates fast or ultrafast internal conversions (IC) to the presence of accessible conical intersections (CI) between the corresponding excited states, implying both electronic energy degeneracy and strong nonadiabatic coupling. In the present situation, the strong fluorescence emission and a relatively long lifetime points, in *anti*-$B_{18}H_{22}$, to a deep S_1 minimum and a CI between S_0 and S_1, $(S_0/S_1)_{CI}$, that cannot be easily accessed with the initially available excess energy (315 nm, 3.93 eV). Our CASPT2//CASSCF calculations have computed the lowest-lying $(S_0/S_1)_{CI}$ energy crossing adiabatically at 299 nm (4.14 eV), representing

dx.doi.org/10.1021/ic201726k | *Inorg. Chem.* 2012, 51, 1471−1479

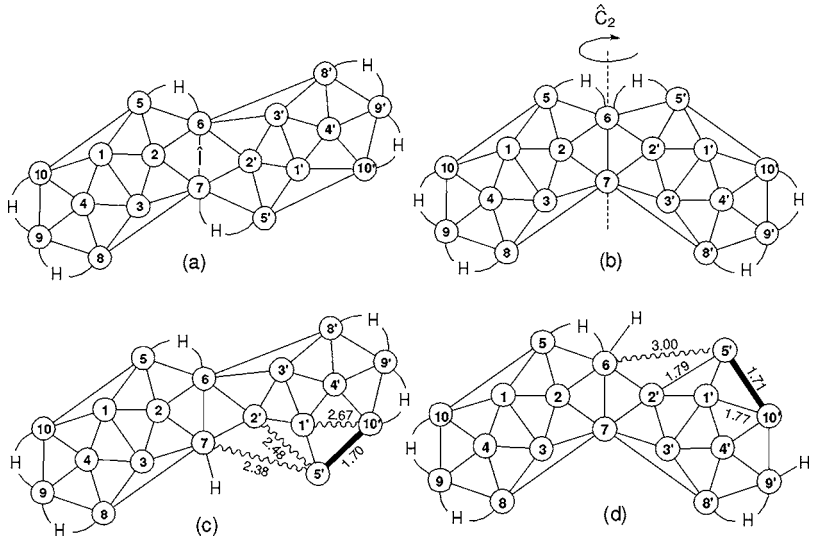

Figure 7. Atom labels for the following: (a) *anti*-$B_{18}H_{22}$ molecular geometry at S_0 ground state, C_i symmetry. Only boron labels are shown together with "bridging" and "*endo*" hydrogen atoms. Terminal hydrogen atoms are omitted for clarity. The inversion operator $\hat{\mathbf{i}}$ (shown in the center of the molecule) relates labels A with A′ → $\hat{\mathbf{i}}$(A) = A′, except for B_6 and B_7, where $\hat{\mathbf{i}}(B_{6,7}) = B_{7,6}$. (b) *syn*-$B_{18}H_{22}$ molecular geometry at S_0 ground state, C_2 symmetry. The $\hat{C}_2$ axis of rotation relates labels A with A′ → $\hat{\mathbf{C}}_2$(A) = A′, except for B_6 and B_7, where $\hat{\mathbf{C}}_2$(A) = A. (c) *anti*-$B_{18}H_{22}$ molecular geometry at $(S_0/S_1)_{CI}$. (d) *syn*-$B_{18}H_{22}$ molecular geometry at $(S_0/S_1)_{CI}$. Significantly elongated B−B connectivities showed as a wavy line, and significantly contracted B−B connectivities as a heavy line, both with respective connectivity distances written in units of angstroms to two decimal places.

an energy barrier of 0.51 eV with respect to the S_1 minimum. The expected sloped structure of the CI is indicative of the decay properties of the *anti* isomer toward the ground state, which is slower and less probable than that in the *syn* species, both because the CI cannot be efficiently reached and because the wave packet is expected to undergo many crossings and recrossings prior to decay toward the ground state, thus explaining the major radiative character of the deactivation and its nanosecond lifetime. Conversely, the *syn* isomer lacks measurable fluorescence emission and displays a much faster picosecond decay. Optimization of the S_1 state of *syn*-$B_{18}H_{22}$ leads to a minimum if the molecular symmetry is restricted to the C_2 point group, and directly to the crossing with the ground state once the system is allowed to break its symmetry. The PEH region close to the minimum and close to the crossing is extremely flat. The calculation of the minimum energy crossing point leads to a $(S_0/S_1)_{CI}$ CI lying adiabatically at 320 nm (3.88 eV) from the ground state minimum. With the consideration that, for the *syn* isomer, the excitation energy to the 1^1B (S_1) state at the FC region is 291 nm (4.26 eV), the system initially has enough excess energy to rapidly and efficiently reach the CI and to decay to the ground state in a nonradiative way, thus explaining the absence of fluorescence emission and the picosecond character of the deactivation pattern observed for the *syn* isomer. A linear interpolation in internal coordinates (LIIC) was performed between these two structures leading to a very small barrier of 1 kcal mol^{-1}. In practice this means that no effective minimum can efficiently trap the energy along the main deactivation path, pointing to a barrierless profile toward the CI.

Triplet States. With regard to the location of the triplet states in *anti*-$B_{18}H_{22}$, the lowest-energy triplet T_1 state lies 0.45 eV below S_1 at the FC region, and, showing a similar relaxation profile than the latter, is placed at the S_1 state minimum 0.50 eV below the singlet state. Singlet state minima are structures favorable for intersystem crossing (ISC) to take place because the energy is trapped for a long enough time to allow ISC processes to occur in competition to generally faster internal conversion (IC) processes. In this case, however, all the triplet states seem, in terms of their respective energies, far apart from S_1. As the system approaches the $(S_0/S_1)_{CI}$ structure, however, the S_1−T_1 energy gap decreases, enhancing the probability for ISC to take place. Although *anti*-$B_{18}H_{22}$ has a high fluorescence quantum yield of 0.97, the additional population of the triplet manifold seems confirmed by the observed ability to produce $O_2(^1\Delta_g)$ in the presence of molecular oxygen. Production of $O_2(^1\Delta_g)$ usually proceeds through photosensitization from a triplet state of a donor system *via* an energy transfer process.[17] The more efficiently the triplet state is populated and the larger the coupling is with the resulting singlet oxygen state, then the higher will be the $O_2(^1\Delta_g)$ production.[18] The state of the donor responsible for the $O_2(^1\Delta_g)$ formation, presumably the T_1 triplet state, has a lifetime of ∼6 μs affording a quantum yield Φ_Δ below 0.01 in hexane solutions. The calculated adiabatic energy for T_1 of the *anti*-$B_{18}H_{22}$ donor is 408 nm (3.04 eV), more than 2 eV higher than the 0.97 eV required to populate the $O_2(^1\Delta_g)$ state through a triplet−triplet energy transfer (TET) mechanism.[17,19] In these cases when the triplet donor lies higher in energy than the final acceptor state the TET process is exothermic and diffusion controlled, with molecular oxygen behaving as a rigid, classical acceptor.[20] Using the computed radiative lifetime for T_1 and low Φ_Δ (<0.01) as a measure of the donor triplet state formation yield, the expected lifetime of the T_1 state of *anti*-$B_{18}H_{22}$ rises to ∼50−500 μs under oxygen-free conditions.

With regards to *syn*-$B_{18}H_{22}$, the 1^1B (S_1) and 1^3A (T_2) states remain close-lying both at the FC structure and the constrained C_2 S_1 minimum, opening the possibility of a favorable ISC especially as the S_1 minimum is not available along the main relaxation path. Considering that the S_1 PEH is somewhat flat near the CI, contributions from an ISC process toward T_1 is not completely unlikely, in particular because the SOC element between S_1 and T_1 is 3.1 cm^{-1}. The evidence of the $O_2(^1\Delta_g)$ formation suggests the involvement of the T_1 triplet states.

dx.doi.org/10.1021/ic201726k | *Inorg. Chem.* 2012, 51, 1471−1479

Geometrical Changes at Stationary Points of the PEH. Figure 7 shows the structure and numbering of (a) *anti*-$B_{18}H_{22}$ (C_i symmetry) and (b) *syn*-$B_{18}H_{22}$ (C_2 symmetry) as proposed by Lipscomb[21] and Todd.[22] The boron atoms related by symmetry operations in these clusters are signified by number/"primed" number pairs. A study of the B−B distance changes in the different stationary points of the PEH was carried out for *anti*-$B_{18}H_{22}$ and *syn*-$B_{18}H_{22}$ as the geometry evolves from the S_0 groundstate to the stationary points T_1, S_1, and $(S_0/S_1)_{CI}$, respectively.

The geometrical change profiles for $S_0 \rightarrow T_1/S_1$ in *anti*-$B_{18}H_{22}$ and *syn*-$B_{18}H_{22}$ are very similar (Figures S5, S6, S8 in the Supporting Information). Given the similar geometrical changes in the $S_0 \rightarrow T_1/S_1$ transitions for both *anti* and *syn* isomers, we include a comprehensive analysis only for the *anti* isomer. We define Δd as the difference between B−B distances in the geometrical change A → B. For *anti*-$B_{18}H_{22}$, the $S_0 \rightarrow T_1/S_1$ changes follow very similar profiles, with a maximum B−B contraction of $\Delta d \sim 0.15/0.13$ Å (T_1/S_1) for B_7−B_8 and the corresponding symmetry-equivalent B_6−$B_{8'}$ (see Figure 7a) followed by values of Δd below 0.10 Å. As for B−B elongations, the maximum value corresponds to B_8−B_9 (and equivalent $B_{8'}$−$B_{9'}$) with $|\Delta d| \sim 0.08$ Å. A close look at Figures S5 and S6 (in the Supporting Information) shows that the profiles are indeed very similar, even in the value of Δd as a function of pairs (B_i, B_j), hence showing that the $S_0 \rightarrow T_1/S_1$ transitions have similar geometrical rearrangements for *anti*-$B_{18}H_{22}$.

In the case of *syn*-$B_{18}H_{22}$, the geometrical change profile for $S_0 \rightarrow T_1$ follows a similar behavior to that of the *anti*-$B_{18}H_{22}$ isomer. The maximum value for B−B shrinkage is in B_7−B_8 (B_7−$B_{8'}$) with $\Delta d \sim 0.12/0.09$ Å (T_1/S_1), the same boron atoms involved as for the *anti*-$B_{18}H_{22}$ isomer. The maximum B−B elongation corresponds to B_5−B_6 with $\Delta d \sim 0.10/0.11$ Å (T_1/S_1), followed by elongations smaller than $\Delta d \sim 0.03$ Å. A comparison between the geometrical change profiles $S_0 \rightarrow T_1$ for the *anti*-$B_{18}H_{22}$ and *syn*-$B_{18}H_{22}$ isomers also shows a similar behavior with slight ordering changes in the bond elongation region, but with similar Δd values ranging from −0.10 Å (elongation) to 0.15 Å (contraction).

The most significant changes in the molecular geometries of both *anti*- and *syn*-$B_{18}H_{22}$ occur at the conical intersection points along their PEH. At these positions the calculated geometries of both isomers are distorted and completely lose their ground state symmetries. Diagrams c and d in Figure 7 illustrate the most significant geometrical changes (also see Figure S7 and S9 in the Supporting Information for complete data): Wavy lines between boron atoms indicate B−B connectivity elongations that extend to clearly nonbonding distances, and heavy lines indicate significant B−B connectivity contractions. Overall, the majority of the B−B connectivity distances for *anti*- and *syn*-$B_{18}H_{22}$ molecules at their $(S_0/S_1)_{CI}$ points remain essentially unchanged from those distances at their S_0 ground states. Significantly, however, the changes that do occur are large and seem to be concentrated in a small number of molecular vibrational modes. In the case of *anti*-$B_{18}H_{22}$ (see Figure 7, diagram c), the most significant geometrical changes are B−B connectivity elongations for B_1−$B_{10'}$ ($\Delta d \sim 0.90$ Å), B_2−$B_{5'}$ ($\Delta d \sim 0.70$ Å), and B_7−$B_{5'}$ ($\Delta d \sim 0.55$ Å), and a B−B contraction along the $B_{5'}$−$B_{10'}$ vector of approximately 0.25 Å. The resulting deformation of the B_7−$B_{2'}$−$B_{5'}$ structural deltahedron leads to disruption of the $H_{7,5'}$ bridging hydrogen (3-center, 2-electron) bond and the establishment of a B−H bond of clear terminal (2-center, 2-electron) character at the B_7 position. The case for *syn*-$B_{18}H_{22}$ (see Figure 7, diagram d) is considerably simpler. Here there is a similar contraction of the $B_{5'}$−$B_{10'}$ connectivity of about 0.26 Å that seemingly disrupts the $H_{9',10'}$ bond to the bridging hydrogen, leaving an *endo*-like 2-center, 2-electron $B_{9'}$−$H_{9'}$ bond in its stead. However, most strikingly of all, the $S_0 \rightarrow (S_0/S_1)_{CI}$ progression for *syn*-$B_{18}H_{22}$ results in only one significant B−B elongation; an approximate increase of 1.2 Å from 1.8 to 3.0 Å in the B_6−$B_{5'}$ connectivity. From a structural perspective, the elongation at the B_6−$B_{5'}$ vector in *syn*-$B_{18}H_{22}$ is rationalized by the high coordination number of the B_6 atom. Uniquely among all the boron atoms in both isomers of $B_{18}H_{22}$, atomic position B_6 from the *syn* isomer coordinates to two bridging hydrogen atoms as well as conjoining the two {*nido*-decaboronyl}-subclusters in the overall 18-vertex cluster structure. The relevant MOs for the *syn*-isomer $(S_0/S_1)_{CI}$ structure are shown in Figure 8. The corresponding natural orbitals are localized, as might be expected, in the B_6−$B_{5'}$ and $B_{5'}$−$B_{10'}$ connectivities. They can be described as the bonding and antibonding counterpart involved in the making/breaking process of the B_6−$B_{5'}$ and the bridging $H_{9',10'}$ bonds.

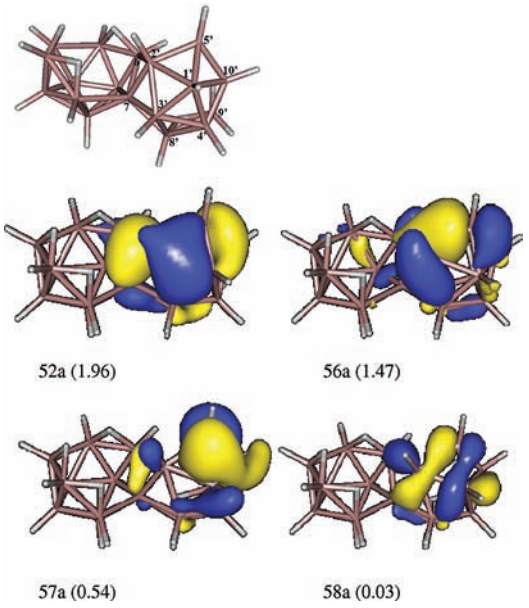

Figure 8. Relevant MOs for the *syn*-$B_{18}H_{22}$ $(S_0/S_1)_{CI}$ structure with occupation numbers shown in parentheses.

Chemically, the $B_{5'}$ position in *syn*-$B_{18}H_{22}$ (that adjacent to atom B_6) is also the site of oxidative ligand substitution to the cluster as is manifest in the structure of [(SMe_2)-*syn*-$B_{18}H_{20}$].[23] From this evidence it is reasonable to surmise that the local coordination strain on atom B_6 may engender a sufficient destabilizing effect on the B_6−$B_{5'}$ connectivity to account for both the chemical reactivity and photophysical properties of *syn*-$B_{18}H_{22}$.

Thus, the distinguishing factor when comparing the geometries of the conical intersections between *anti*-$B_{18}H_{22}$ and *syn*-$B_{18}H_{22}$ is the presence of a conspicuous B−B elongation of well above 1 Å when compared to the S_0 ground state geometry for *syn*-$B_{18}H_{22}$. The *anti*-$B_{18}H_{22}$ isomer also undergoes significant elongations for $(S_0/S_1)_{CI}$, but in this case, several B−B connectivities are below 1 Å, such that the absorbed energy in S_1 is redistributed vibrationally into several regions of the molecule rather than (almost completely) into a

dx.doi.org/10.1021/ic201726k | *Inorg. Chem.* 2012, 51, 1471−1479

single vibrational mode, as in *syn*-$B_{18}H_{22}$, allowing for a minimum in the S_1 PEH (Figure 6a).

CONCLUSION

The combined experimental and computational work in this report, for the first time, rationalizes the known observation that the *anti* isomer of molecular boron hydride $B_{18}H_{22}$ displays an intense fluorescence whereas its *syn* isomer shows no such activity. We show that the measured first singlet excited state S_1 lifetime in *anti*-$B_{18}H_{22}$ is 2 orders of magnitude longer than in the corresponding *syn* isomer and that the latter decays nonradiatively on a picosecond time scale. Calculations show that the difference in the geometries of the two isomers at the conical intersection points along their PEHs is the key determining factor in their different decay processes.

Our current work is focused on the synthesis of derivatives of the isomers of $B_{18}H_{22}$ with cluster substituents that do not alter the overall cluster geometries of the boron hydride compounds. Small changes to the molecules are expected to affect the photophysics of the 18-vertex borane systems. In particular, we are interested in manipulation of the energy differences between S_1 minima and $(S_0/S_1)_{CI}$ points to increase the probability for efficient spin−orbit coupling between singlet and triplet excited states that eventually give rise to singlet-oxygen production. Preliminary experimental results, on which we intend to report shortly, suggest that such manipulation of photophysical properties through simple chemical molecular alterations is indeed possible.

ASSOCIATED CONTENT

Supporting Information

UV−vis spectra, kinetic data, additional computational details, and Cartesian coordinates of the optimized geometries for *anti*- and *syn*-$B_{18}H_{22}$ at points along the PEH as well as graphs showing the B−B connectivity elongations and contractions for these geometries. This material is available free of charge via the Internet at http://pubs.acs.org.

AUTHOR INFORMATION

Corresponding Author

*E-mail: michaell@iic.cas.cz (M.G.S.L.); j.m.oliva@iqfr.csic.es (J.M.O.); hnyk@iic.cas.cz (D.H.); lang@iic.cas.cz (K.L.).

ACKNOWLEDGMENTS

This research was supported by the Czech Science Foundation (Nos. P207/11/1577 and P208/10/1678), Czech Ministry of Education (MSM6007665808), and Spanish Projects CTQ2010-14892, CSD2007-0010 Consolider-Ingenio in Molecular Nanoscience, Comunidad de Madrid Project S2009/ESP/1691 Program MODELICO-CM, and European Union Projects FP7-ICT-2009-4-248909-LIMA and FP7-ICT-2009-4-248855-N4E. The authors would like to thank to Marcel Fuciman and Pavel Chábera (University of South Bohemia, Nové Hrady) for technical help with femtosecond experiments. We also thank Professor Manuela Merchán (Valencia) for reading the manuscript and are grateful to Professor Ulises Acuña (Madrid) for helpful general discussions. We also thank Professor J. I. Burgos for helpful discussions regarding the analyses of geometrical changes of the stationary points for the PEHs.

REFERENCES

(1) Kawasaki, Y.; Kuroi, T.; Yamashita, T.; Horita, K.; Hayashi, T.; Ishibashi, M.; Togawa, M.; Ohno, Y.; Yoneda, M.; Horsky, T.; Jacobson, D.; Krull, W. *Nucl. Instrum. Meth. B* **2005**, *237*, 25.
(2) Londesborough, M. G. S.; Bould, J.; Baše, T.; Hnyk, D.; Bakardjiev, M.; Holub, J.; Císařová, I.; Kennedy, J. D. *Inorg. Chem.* **2010**, *49*, 4092.
(3) Pitochelli, A. R.; Hawthorne, M. F. *J. Am. Chem. Soc.* **1962**, *84*, 3218.
(4) Volkov, V. V.; Il'inchik, E. A.; Volkov, O. V.; Yuryeva, O. O. *Chem. Sustainable Dev.* **2000**, *8*, 185.
(5) (a) Plešek, J.; Heřmánek, S.; Štíbr, B.; Hanousek, F. *Collect. Czech. Chem. Commun.* **1967**, *32*, 1095. (b) Li, Y.; Sneddon, L. G. *Inorg. Chem.* **2005**, *45*, 470.
(6) Lakowicz, J. R. In *Principles of Fluorescence Spectroscopy*; Kluwer Academic/Plenum, New York: 1999.
(7) Rossbroich, G.; Garcia, N. A.; Braslavsky, S. E. *J. Photochem.* **1985**, *31*, 37.
(8) (a) Andersson, K.; Malmqvist, P. A.; Roos, B. O. *J. Chem. Phys.* **1992**, *96*, 1218. (b) Andersson, K.; Malmqvist, P. A.; Roos, B. O.; Sadlej, A. J.; Wolinski, K. *J. Phys. Chem.* **1990**, *94*, 5483. (c) Roos, B. O.; Andersson, K.; Fulscher, M. P.; Malmqvist, P. A.; Serrano-Andrés, L.; Pierloot, K.; Merchán, M. *Adv. Chem. Phys.* **1996**, *93*, 219.
(9) (a) Serrano-Andrés, L.; Merchán, M.; Nebotgil, I.; Lindh, R.; Roos, B. O. *J. Chem. Phys.* **1993**, *98*, 3151. (b) Serrano-Andrés, L.; Merchán, M.; Lindh, R. *J. Chem. Phys.* **2005**, 122.
(10) (a) Rubio-Pons, O.; Serrano-Andrés, L.; Merchán, M. *J. Phys. Chem. A* **2001**, *105*, 9664. (b) Strickler, S. J.; Berg, R. A. *J. Chem. Phys.* **1962**, *37*, 814.
(11) (a) Malmqvist, P. A.; Roos, B. O.; Schimmelpfennig, B. *Chem. Phys. Lett.* **2002**, *357*, 230. (b) Merchán, M.; Serrano-Andrés, L.; Robb, M. A.; Blancafort, L. *J. Am. Chem. Soc.* **2005**, *127*, 1820.
(12) Pople, J. A. In *Gaussian 03*; Gaussian, Inc: Wallingford, CT, 2004.
(13) Lindh, R.; Aquilante, F.; De Vico, L.; Ferre, N.; Ghigo, G.; Malmqvist, P. A.; Neogrady, P.; Pedersen, T. B.; Pitonak, M.; Reiher, M.; Roos, B. O.; Serrano-Andrés, L.; Urban, M.; Veryazov, V. *J. Comput. Chem.* **2010**, *31*, 224.
(14) Mains, G. J. *J. Phys. Chem.* **1991**, *95*, 5089.
(15) Wilkinson, F.; Helman, W. P.; Ross, A. B. *J. Phys. Chem. Ref. Data* **1993**, *22*, 113.
(16) (a) Platt, J. R. *J. Chem. Phys.* **1949**, *17*, 484. (b) Serrano-Andrés, L.; Roos, B. O. *J. Am. Chem. Soc.* **1996**, *118*, 185.
(17) Lang, K.; Mosinger, J.; Wagnerová, D. M. *Coord. Chem. Rev.* **2004**, *248*, 321.
(18) Serrano-Andrés, L.; Serrano-Perez, J. J.; Olaso-Gonzalez, G.; Merchán, M. *Chem. Phys.* **2009**, *360*, 85.
(19) Bonnett, R. *Chem. Soc. Rev.* **1995**, *24*, 19.
(20) Frutos, L. M.; Castano, O. *J. Chem. Phys.* **2005**, 123.
(21) (a) Simpson, P. G.; Lipscomb, W. N. *Proc. Natl. Acad. Sci. U.S.A.* **1962**, *48*, 1490. (b) Simpson, P. G.; Lipscomb, W. N.; Folting, K. *J. Am. Chem. Soc.* **1963**, *85*, 1879.
(22) Todd, L. J. *Pure. Appl. Chem.* **1972**, *30*, 587.
(23) Jelínek, T.; Grüner, B.; Císařová, I.; Štíbr, B.; Kennedy, J. D. *Inorg. Chem. Commun.* **2007**, *10*, 125.